Dalton Transactions

The controlling role of atmosphere in dawsonite versus gibbsite precipitation from tetrahedral aluminate species

Journal:	*Dalton Transactions*
Manuscript ID	DT-ART-06-2021-002081.R1
Article Type:	Paper
Date Submitted by the Author:	17-Aug-2021
Complete List of Authors:	Dembowski, Mateusz; Pacific Northwest National Laboratory Loring, John; Pacific Northwest National Laboratory Bowden, Mark; Pacific Northwest National Laboratory Reynolds, Jacob; Washington River Protection Solutions LLC Graham, Trent; Pacific Northwest National Laboratory Rosso, Kevin; Pacific Northwest National Laboratory Pearce, Carolyn; Pacific Northwest National Laboratory; Washington State University, Department of Crop and Soil Sciences

The controlling role of atmosphere in dawsonite versus gibbsite precipitation from tetrahedral aluminate species

Mateusz Dembowski[†], John S. Loring[†], Mark Bowden[†], Jacob G. Reynolds[‡], Trent R. Graham[†], Kevin M. Rosso[†], and Carolyn I. Pearce[†, #]

[†]Pacific Northwest National Laboratory, Richland, Washington 99352, USA

[‡]Washington River Protection Solutions, LLC, Richland, Washington 93352, USA

[#] Washington State University, Pullman, WA, 99164

Abstract

In highly alkaline solution, aluminum speciates as the tetrahedrally coordinated aluminate monomer, $Al(OH)_4^-$ and/or dimer $Al_2O(OH)_6^{2-}$, yet precipitates as octahedrally coordinated gibbsite ($Al(OH)_3$). This tetrahedral to octahedral transformation governs Al precipitation, which is crucial to worldwide aluminum (Al) production, and to the retrieval and processing of Al-containing caustic high-level radioactive wastes. Despite its significance, the transformation pathway remains unknown. Here we explore the roles of atmospheric water and carbon dioxide in mediating the transformation of the tetrahedrally coordinated potassium aluminate dimer salt ($K_2Al_2O(OH)_6$) to gibbsite versus potassium dawsonite ($KAl(CO_3)(OH)_2$). A combination of in-situ attenuated total reflection infrared spectroscopy, ex-situ micro X-ray diffraction, and multivariate curve resolution-alternating least squares chemometrics analysis reveals that humidity plays a key role in the transformation by limiting the amount of alkalinity neutralization by dissolved CO_2. Lower humidity favors higher alkalinity and incorporation of carbonate species in the final Al product to form $KAl(CO_3)(OH)_2$. Higher humidity enables more acid generation that destabilizes dawsonite and favors gibbsite as the solubility limiting phase. This indicates that the transition from tetra- to octahedrally coordinated Al does not have to occur in bulk solution, as has often been hypothesized, but may instead occur in thin water films present on mineral surfaces in humid environments. Our findings suggest that phase selection can be controlled by

humidity, which could enable new pathways to Al transformations useful to the Al processing industry, as well as improved understanding of phases that appear in caustic Al-bearing solutions exposed to atmospheric conditions.

Introduction

In highly alkaline aqueous solution, the coordination chemistry of aluminum and mechanisms controlling its precipitation remain incompletely understood, despite their importance across many contexts. For example, gibbsite ($Al(OH)_3$) precipitation from concentrated caustic solutions is a fundamental step in the production of the world's supply of alumina (Al_2O_3) and Al-based products from bauxite ore through the Bayer process, developed in 1888.[1-3] Similarly, dissolution and reprecipitation of gibbsite is of primary importance in the major environmental remediation efforts at legacy nuclear sites in the United States including the Hanford and Savannah River Sites.[4, 5] At Hanford, an estimated 56 million gallons of radioactive waste, in the form of supernatant liquid, sludges, and saltcake solids, contain an abundance of aluminum oxyhydroxide solids such as gibbsite in highly caustic sodium hydroxide solution.[6-8] The highly caustic, and aluminum rich nature of these waste streams arises from additions of NaOH and $Al(NO_3)_3$ to maintain a high pH and sequester fluoride, respectively, to prolong the life of the steel tanks in which the waste is stored.[9, 10] Processing of these wastes for safe disposal relies in part on limiting what are still relatively large uncertainties in the precipitation kinetics of gibbsite during processing.

Across these highly alkaline contexts, at the molecular scale precipitation of aluminum phases is largely characterizable as predicated upon a coordination change from the tetrahedrally coordinated aluminate anion $[Al(OH)_4]^-$ in solution to what is typically octahedral aluminum coordination in precipitated aluminum solids. Besides gibbsite, other relevant six-coordinate Al phases include boehmite (AlO(OH)) and, in the presence of atmospheric CO_2, carbonate-containing sodium dawsonite ($NaAl(CO_3)(OH)_2$).[10] Dawsonite is of particular interest in the context of radioacitve wastes because it was recently identified as a cementing agent in an indurated crust that formed over two decades of air exposure.[11, 12] Recent laboratory experiments have shown that the precipitation of gibbsite, boehmite, and/or dawsonite can be accelerated by CO_2, resulting in a complex precipitation pathway involving multiple aluminum hydroxide and oxyhydroxide phases.[13-15] Due to the instability of six-coordinate Al species such as $Al(H_2O)_6^{3+}$, Al_8 or Al_{13} under caustic conditions, the mechanism of gibbsite precipitation has been hypothesized to proceed via formation of $Al(OH)_6^{3-}$ species, or $Al(OH)_6^{3-}$ related oligomeric

precursors,[16] leading to nucleation and growth. However, attempts at detecting the $Al(OH)_6^{3-}$ species have been unsuccessful and are documented in the literature.[17-21] It is likely that the nucleation and growth of gibbsite in basic solutions is mechanistically dissimilar from gibbsite formed under circumneutral conditions, such as during synthesis from pH-neutralized aluminum nitrate solutions, where the transformation occurs through an amorphous aluminum hydroxide intermediate.[22] Furthermore, when CO_2 is present, it remains unknown whether its accelerating effect arises from its involvement in forming precursor complexes or from its ability to locally reduce the pH of the highly alkaline system.[23]

The present study focuses on improving understanding of the effect of atmospheric CO_2 and water on the precipitation of gibbsite versus dawsonite in highly alkaline solutions. To control the speciation of the source of the aluminate anion while also limiting the counterion composition to a single alkali cation, we specifically examine the transformation of the potassium aluminate salt $K_2Al_2O(OH)_6$ to potassium dawsonite $KAl(CO_3)(OH)_2$ and/or gibbsite. The potassium aluminate salt structure is based on an aluminate dimer motif that is well characterized both in the solid and in alkaline solutions.[20, 21] Based on recent reports that correlate higher quantities of aluminate dimer in solution with more extensive gibbsite nucleation,[20] and the presence of aluminate dimer-like structures during precipitation of octahedrally coordinated sodium aluminate hydroxy hydrates ($Na_9[Al(OH)_6]_2{\cdot}3(OH){\cdot}6(H_2O)$),[17] the reactivity of tetrahedrally coordinated aluminate dimers can provide insight into the Al coordination change mechanism. We control the relative humidity of a constant CO_2 reaction atmosphere to explore the effect of water availability in facilitating the phase transformation. A combination of in-situ attenuated total reflection-infrared spectroscopy and ex-situ micro X-ray diffraction measurements provided time-resolved insights into the transformation pathway, including identification of intermediates, products, and their dependence on changing atmospheric conditions. The results point to the importance of acidification from dissolved CO_2 in determining selection of product phases and their kinetics of precipitation.

Experimental

Synthesis of $K_2Al_2O(OH)_6$. Crystalline $K_2Al_2O(OH)_6$ has been prepared in accordance with prior literature reports.[21, 24] Purity of obtained material was assessed using combination of Raman spectroscopy and powder X-ray diffraction.

In situ Infrared (IR) spectroscopy. IR spectra were collected using a FastIR (Harrick Scientific) attenuated total reflection (ATR) cell with a single-reflection zinc selenide internal reflection element (IRE) and a custom-built flow attachment. The spectrometer was a Bruker Vertex 80v with an air-cooled source and a deuterated triglycine sulfate detector. Spectra were an average of 128 scans at 4 cm^{-1} resolution between 600 and 5000 cm^{-1}. Background single-channel spectra were of the clean IRE under argon flow. Sample single-channel spectra were collected as a function of time from an overlayer of $K_2Al_2O(OH)_6$ on the IRE reacting under humidified argon with 400 ppm CO_2. Sample absorbance spectra were calculated using the negative decadent logarithm of the ratio of the sample to the background single-channel spectra. The overlayer was prepared by evaporating a suspension of $K_2Al_2O(OH)_6$ in acetonitrile onto the IRE under argon.

Experiments were performed at relative humidity (RH) values of 20, 30, 40, 50 and 60%. RH was controlled by an automated mass flow controller apparatus. This system was comprised of two mass flow controllers (Alicat Scientific) and a solid-state humidity sensor (Vaisala). One mass flow controller was dedicated to anhydrous gas, while the other controlled the flow of gas that was nearly saturated with H_2O by flow through a semipermeable nafion tube (Permapure) immersed in degassed water. The combined gas streams flowed over the humidity sensor. The ratio of the flow rate of the two mass flow controllers was controlled in real time using custom software that utilized feedback from the humidity sensor, providing constant flow at a target relative humidity. The total flow rate was 200 cm^3/min. Replicates performed at 40 and 60% RH demonstrated reproducibility of our experimental approach.

Spectra from experiments at each RH were processed to correct for baseline drift by fitting a linear baseline, as well as to remove H_2O vapor and CO_2 that arise due to changes in these gas concentrations in the spectrometer chamber. They were also normalized so that they have the same area between 620 and 3720 cm^{-1}. Data sets were then analyzed over this same spectral range by a multivariate curve resolution-alternating least squares (MCR-ALS)

chemometrics analysis that uses a non-negativity constraint in both spectral and concentration space. In an MCR-ALS analysis, the measured spectra are assumed to be a linear combination of spectral components, and both the absorbances and the concentrations of the spectral components are calculated.[25, 26] The spectral components are linearly independent spectra resolved by MCR-ALS, and they could be comprised of the spectra of more than one chemical species that covary with time. The analyses performed here were to help simplify and visualize trends in the datasets. Consistent solutions were targeted in the spectra and concentrations of the components and their concentrations across the datasets from 20 to 60% RH that provided a chemically legitimate interpretation. The analyses are not intended to be strict quantifications of the datasets.

The number of spectral components for the 20, 30, and 60% RH data sets were chosen based on a singular value decomposition (SVD) of these data sets. Ideally, an SVD can delineate the number of components that model real data from the number that model noise based on the percentage of the variance accounted by the components. The criterion we used is that the number of components that model real data is indicated by a ten-fold delineation in the percentage of the variance of successive eigenvectors computed from the singular values outputted from an SVD. While this method for determining components worked well for 20, 30, and 60% RH data sets, the 40% and 50% RH results were less clear. Specifically, for the 40 and 50% RH data, there was no clear ten-fold delineation in component percentage of variance. Hence, for these data sets, we chose the number of components to be consistent with the trends in the chemistry resolved by μXRD and the analyses in the 20, 30, and 60% RH data sets.

Micro powder X-ray diffraction (μ-pXRD). Post-reacted samples removed from the IRE at the end of in situ IR experiments were loaded into 0.5 mm diameter thin-walled glass capillaries (Charles Supper Co., MA) and sealed with wax to prevent reaction with ambient gas. The capillaries were positioned in a Rigaku D/MAX Rapid II microbeam diffractometer fitted with a rotating Cr anode source (λ = 2.2910 Å) operated at 35 kV and 25 mA and focused through a 0.3 mm diameter collimator. Data were collected over a 5-minute exposure on a large 2D image plate and subsequently integrated between 10 and 150° 2θ using proprietary Rigaku software to give 1D diffractograms. The crystalline phases present were identified by comparison with reference

patterns from the International Center for Diffraction Data using JADE (Materials Data Inc., CA). For each sample data collection was initiated within 30 minutes of ending the in-situ experiment.

Results and Discussion

The reaction of solid $K_2Al_2O(OH)_6$ in gaseous CO_2 (400 ppm in argon) was followed as a function of time using in-situ ATR IR spectroscopy at RH values of 20, 30, 40, 50, and 60% to investigate the effect of H_2O on the transformation products and their rates of formation. Post-reacted samples were further analyzed ex-situ using µXRD. Because the RH at Hanford varies from ca. 77% in winter to ca. 36% during summer,[27] we focus in the main text on data collected at 40, 50, and 60% RH. Experimental results for 20, and 30% RH (**Figure S1**, **S2**) are available in the **Supporting Information**.

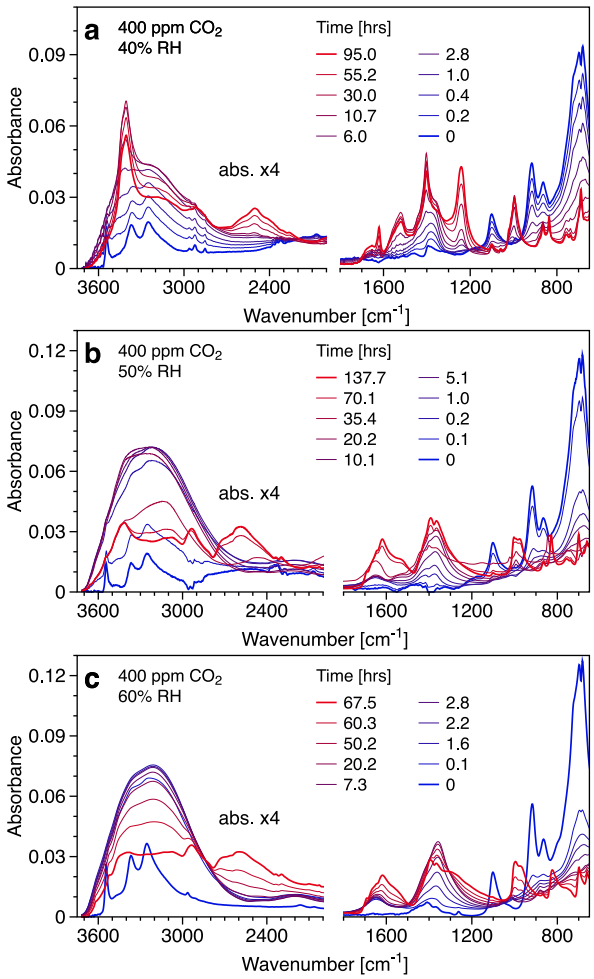

Figure 1. Examples of ATR IR spectra from 650 to 3700 cm^{-1} as a function of time during the reaction of $K_2Al_2O(OH)_6$ in a gas mixture of 400 ppm CO_2 in argon at 25°C and RH values of (a) 40%, (b) 50%, and (c) 60%. Spectra have been baseline corrected and area normalized, as described in the Methods section. Note the scale change between low (650-1800 cm^{-1}) and high (2000-3750 cm^{-1}) wavenumber region.

Figure 1 shows area normalized ATR IR spectra from experiments at 40, 50, and 60% RH at reaction times that highlight major temporal reactivity trends. Unreacted $K_2Al_2O(OH)_6$ (spectra at 0 hr reaction time) exhibits bands at 680, 698, 862, 914, 1099 cm^{-1} that are due to Al-O stretching and Al-O-H bending vibrations, as well as peaks at 3253, 3363, and 3542 cm^{-1} assigned to OH stretching motions.[21, 28] Notably, $K_2Al_2O(OH)_6$ does not react when exposed to anhydrous 400 ppm CO_2, but rapidly transforms with exposure to humidity and adsorption of H_2O. Bands corresponding to the Al-O stretches and Al-O-H bends of $K_2Al_2O(OH)_6$ decrease in intensity. The new bands that grow in can be summarized as predominantly: (i) the C-O stretches (1050 to 1650 cm^{-1}) and CO_3 deformations (620 to 850 cm^{-1}) of (bi)carbonate moieties; (ii) the H-O-H bend of adsorbed H_2O and structural H_2O in transformation products (between 1550 and 1650 cm^{-1}); (iii) the OH stretches of adsorbed and structural H_2O and Al bound hydroxyls (2900 to 3700 cm^{-1}); and (iv) the OH stretches diagnostic of hydroxyls of bicarbonate (2200 to 3000 cm^{-1}).[29, 30]

The relative intensity of bands corresponding to H_2O increases with increasing RH, particularly during the first few hours of the experiments. After an hour of reaction at 60% RH, the IR spectrum resembles that of an aqueous solution containing dissolved CO_3^{2-} (CO stretch at 1400 cm^{-1}), indicating sufficient H_2O adsorption led to deliquescence. At 40% RH (and below), the H_2O bands are much less dominant, with the H_2O likely adsorbed as a thin film, perhaps only monolayers in thickness. The spectra from the intermediate 50% RH experiment are initially dominated by the spectrum of H_2O. At longer reaction times, the intensity of the H_2O bands eventually decreases, indicating that the reaction products at longer times have less structural water, or are more hydrophobic, leading to H_2O desorption. No signals consistent with presence of dissolved aluminate species (i.e. $Al(OH)_4^-$, $Al_2O(OH)_6^{2-}$) were observed in any of the considered systems, likely due to the relatively weak Al-O based vibrations compared to other species with higher absorption coefficients (e.g. K_2CO_3).

Table 1. Summary of crystallographic phases identified at different RH conditions following ex-situ µXRD analysis. The nine-digit numbers located below the chemical formulas of individual phases correspond to their entries within the International Centre for Diffraction Data (ICDD) database. Final pH of the system was approximated on the basis of carbonate speciation and the identity of co-products.

	crystallographic phases						
Relative Humidity	$K_2Al_2O(OH)_6$ 04-012-6223	$KAl(CO_3)(OH)_2$ 04-012-1124	$Al(OH)_3$ 00-033-0018	$KHCO_3$ 01-089-2369	K_2CO_3 04-010-8931	$K_4H_2(CO_3)_3$ 04-018-3635	final pH*
40%	Abs.	Pr.	Pr.	Pr.	Pr.	Pr.	8-10
50%	Abs.	Pr.	Pr.	Pr.	Abs.	Pr.	7-8

60%	Abs.	Abs.	Pr.	Pr.	Abs.	Abs.	7-8

Pr. = present, Abs. = absent, final pH* of the system was approximated on the basis of carbonate speciation (ref. 36).

The time dependence of the IR spectra in **Figure 1** is complex and suggests phase evolution involving several transformation intermediates. To help identify the phases present after a reaction time of 500, 260, 90, 140, and 70 hours for 20, 30, 40, 50, and 60% RH, respectively, the post-reacted solids were collected from the ATR IR cell and analyzed by μXRD. The crystalline phases present are listed in **Table 1**. Due to the small sample size (ca. 5 mg), large crystallite size, and lack of internal standard, the XRD results could not be quantified. Irrespective of RH conditions the products of the reaction between $K_2Al_2O(OH)_6$ and CO_2 can be grouped into Al-bearing ($KAl(CO_3)(OH)_2$ [04-012-1124], $Al(OH)_3$ [00-033-0018]) and Al-free ($K_2CO_3{\cdot}1.5H_2O$ [04-010-8931], $K_4H_2(CO_3)_3{\cdot}1.5H_2O$ [04-018-3635], $KHCO_3$ [01-089-2369]) phases.

The Al-free phases show a strong dependence on RH, with the most basic $K_2CO_3{\cdot}1.5H_2O$ dominating at RH≤40%, the mixed carbonate-bicarbonate $K_4H_2(CO_3)_3{\cdot}1.5H_2O$ present at 30%≤RH≤50%, and the most acidic $KHCO_3$ becoming prevalent at RH≥40% (**Table 1**). The presence of structural carbonate in Al-bearing phases also demonstrates a dependance on RH. Specifically, $KAl(CO_3)(OH)_2$ is more prevalent at RH≤50% while $Al(OH)_3$ is only observed at RH≥40%. Hence, carbonate containing $KAl(CO_3)(OH)_2$ tended to coprecipitate with the Al-free $K_2CO_3{\cdot}1.5H_2O$ and $K_4H_2(CO_3)_3{\cdot}1.5H_2O$ species. The $KAl(CO_3)(OH)_2$ phase was not detected when the only Al-free product was potassium bicarbonate, $KHCO_3$.

Identification of crystalline post-reaction products using μXRD permitted further analysis of the time-resolved ATR-IR spectroscopic results (**Figure 1**). In particular, the (bi)carbonate phases listed in **Table 1** undoubtedly account for many of the emerging signals in the 1200-1800 cm^{-1} spectral region.[31-33] A multivariate curve resolution alternating least squares (MCR-ALS) approach was used to simplify the IR results into a linear combination of a small number of spectral components so that reaction pathways could be elucidated. Analyses were performed on the area normalized data sets at each RH in the spectral range from 620 to 3720 cm^{-1}. The number of spectral components used for each RH system was based on several factors, including the number of solid phases detected by μXRD, the number of components indicated by a singular value decomposition (SVD) of the data (see Methods), and considering the number of

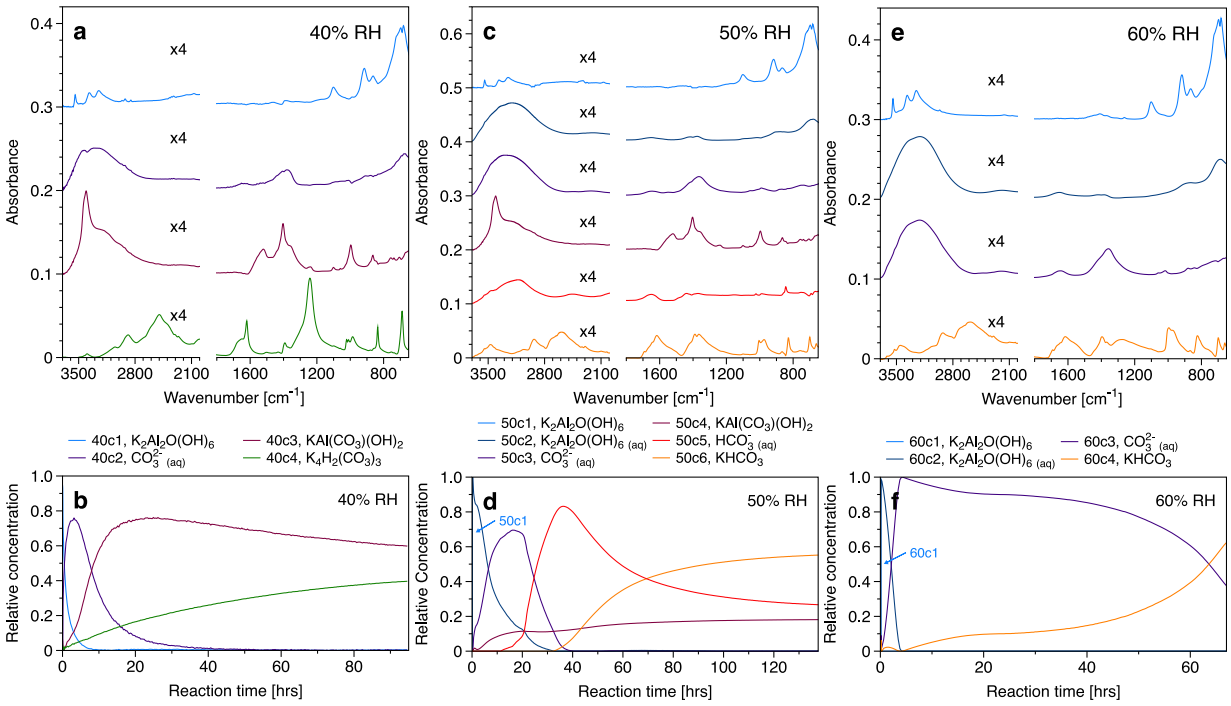

Figure 2. Results of MCR-ALS analyses of ATR IR spectra collected as a function of time during experiments where $K_2Al_2O(OH)_6$ was reacted in a gas mixture of 400 ppm CO_2 in argon at 25°C. Panels (a) and (b) show the spectra and relative concentrations, respectively, of the components resolved for the experiment carried out at 40% RH. Likewise, panels (c) and (d) are from the experiment at 50% RH, and (e) and (f) at 60% RH. Assignments are given in the legends, and the same color is used in all experiments for components assigned to the same species. The MCR-ALS analyses accounted for better than 99.95% of the variance in the data at each RH.

components indicated by experimental analyses at adjacent RH values. **Figure 2** summarizes the MCR-ALS resolved spectral components in the range from 650 to 1800 cm^{-1} and 2000 to 3700 cm^{-1}, as well as their relative concentrations as a function of time, for experiments at 40, 50, and 60% RH. The MCR-ALS results for the experiments at 20 and 30% RH (**Figure S3**) are available in **Supporting Information**.

40% relative humidity

Four spectral components were used for the MCR-ALS analysis of the ATR IR data at 40% RH (**Figure 1a**), and their spectra are shown in **Figure 2a**. Component 40c1 is the spectrum of the unreacted $K_2Al_2O(OH)_6$ aluminate dimer, which is present in the MCR-ALS at each RH investigated. Based on the presence of the characteristic ν_3 asymmetric CO_3 stretching vibration at ca. 1400 cm^{-1} and the H_2O bending mode of water at ca. 1640 cm^{-1}, the second component, 40c2, is assigned to aqueous carbonate, $CO_3^{2-}{}_{(aq)}$ present in H_2O adsorbed on the $K_2Al_2O(OH)_6$ surface.[34, 35] In addition, the broad absorbance between 650-1000 cm^{-1} indicates that the 40c2

component also contains a spectral contribution from partially solvated/hydrated $K_2Al_2O(OH)_6$ (see discussion of results for 50 and 60% RH below). The spectrum of 40c3 is assigned to $KAl(CO_3)(OH)_2$, as identified by μXRD (**Table 1**), and based on an Al-OH deformation at 997 cm^{-1}, characteristic ν_2 CO_3^{2-} signatures at 759 and 865 cm^{-1}, and a uniquely strong O-H vibration at 3440 cm^{-1}.[33, 36] The fourth component is assigned to the $K_4H_2(CO_3)_3 \cdot 1.5H_2O$ phase detected by μXRD (**Table 1**), which is characterized by a C-O-H bend at 1240 cm^{-1}, and a weak ν_3 asymmetric CO_3^{2-} vibration at 1392 cm^{-1}.[37] Transition from carbonate-rich to mixed carbonate/bicarbonate species suggests a progressive shift from pH > 10 to 8 < pH < 10.[38]

Figure 2b summarizes changes in relative concentrations of the four spectral components (40c1-4) as a function of time for the experiment at 40% RH. The trends in the concentrations, rather than the actual absorption coefficients, are the focus in **Figure 2b**, because the MCR-ALS analyses were carried out on area normalized measured spectra and the absorption coefficients of the components were assumed to be identical. Exposure of $K_2Al_2O(OH)_6$ (40c1) to 400 ppm CO_2 at 40% RH leads to its rapid depletion (0-10 hrs) and congruent growth of the $CO_3^{2-}{}_{(aq)}$ component (40c2). This can be explained by the decomposition of $K_2Al_2O(OH)_6$ through reaction with H_2O to produce caustic potassium hydroxide (KOH) and an amorphous Al-hydroxide phase:

$$K_2Al_2O(OH)_6 + H_2O \rightarrow 2KOH + 2Al(OH)_3^{am} \qquad \text{Eq. 1}$$

The Al-hydroxide product in Eq. 1 is assumed to be amorphous because no unique O-H stretching bands were observed that would identify this as a crystalline phase, e.g., gibbsite,[39] although these O-H stretching bands could be below the detection limit. The dissolved hydroxide produced from the KOH product in Eq. 1 can react with carbon dioxide:

$$2KOH + CO_2 \rightarrow K_2CO_3 + H_2O \qquad \text{Eq. 2}$$

to yield potassium carbonate/carbonate anions. Formation of carbonate at the expense of potassium hydroxide is consistent with the experimental observation showing direct, but inverse relationship between the relative concentrations of $K_2Al_2O(OH)_6$ and $CO_3^{2-}{}_{(aq)}$. After about 10

hours of reaction, the relative concentration of $CO_3^{2-}{}_{(aq)}$ (40c2) begins to decrease and is no longer detected by 40 hours. The decrease in $CO_3^{2-}{}_{(aq)}$ coincides with the growth of $KAl(CO_3)(OH)_2$ (40c3, rapid) and $K_4H_2(CO_3)_3{\cdot}1.5H_2O$ (40c4, slow). Formation of $KAl(CO_3)(OH)_2$ (40c3) could occur by the following reaction with K_2CO_3:

$$Al(OH)_3^{am} + K_2CO_3 \rightarrow KAl(CO_3)(OH)_2 + KOH \quad \text{Eq. 3}$$

with release of KOH promoting formation of additional K_2CO_3 according to Eq. 2. This is consistent with the trend in **Figure 2b**, where a slower (5-40 hrs) decline in the concentration of $CO_3^{2-}{}_{(aq)}$ follows the rapid initial growth (0-5 hrs). Formation of $K_4H_2(CO_3)_3{\cdot}1.5H_2O$ requires generation of the bicarbonate anion (HCO_3^-), via the reaction:

$$CO_2 + CO_3^{2-} + H_2O \leftrightarrow 2HCO_3^- \quad \text{Eq. 4}$$

which is consistent with the loss of $CO_3^{2-}{}_{(aq)}$ at the time that $K_4H_2(CO_3)_3{\cdot}1.5H_2O$ precipitates. The series of equations to precipitate $K_4H_2(CO_3)_3{\cdot}1.5H_2O$ (40c4) from CO_2 and K_2CO_3 are:[40-42]

$$K_2CO_3 + 1.5H_2O \rightarrow K_2CO_3 \cdot 1.5H_2O \quad \text{Eq. 5}$$

$$2K_2CO_3 \cdot 1.5H_2O + CO_2 \rightarrow K_4H_2(CO_3)_3 \cdot 1.5H_2O + 0.5H_2O \quad \text{Eq. 6}$$

With increasing time, more CO_2 is consumed as a reactant, resulting in gradual increase in acidity thereby shifting the equilibrium towards formation of $K_4H_2(CO_3)_3{\cdot}1.5H_2O$ (40c4).

The μXRD analysis of the post-reacted sample from the 40% RH experiment confirmed complete reaction of $K_2Al_2O(OH)_6$ (40c1) and formation of not only $KAl(CO_3)(OH)_2$ (40c3) but also gibbsite, $Al(OH)_3$, as Al-bearing products (**Figure S4**). Gibbsite might form from the re-arrangement of amorphous Al-hydroxide produced during initial decomposition of $K_2Al_2O(OH)_6$ (Eq.1):

$$Al(OH)_3^{am} \rightarrow Al(OH)_3^{gib} \quad \text{Eq. 7}$$

The IR spectra of the four components resolved by the MCR-ALS analysis, and a spectrum of the post-reacted sample collected immediately prior to μXRD measurement (**Figure S5**), did not exhibit signals consistent with gibbsite. In the ATR IR spectra, the absorption coefficients of the bands associated with carbonate-containing phases are much larger than those of the carbonate-free phases, therefore the lack of characteristic gibbsite signatures is likely because they are swamped by those of $KAl(CO_3)(OH)_2$ (40c3) and $K_4H_2(CO_3)_3{\cdot}1.5H_2O$ (40c4).[39] Other crystalline phases, including $K_2CO_3{\cdot}1.5H_2O$ and $KHCO_3$, are present in the μXRD results for the products of the reaction at 40% RH, but the bands for these species are hidden behind more intense bands for $KAl(CO_3)(OH)_2$ and $K_4H_2(CO_3)_3{\cdot}1.5H_2O$, assigned as 40c3 and 40c4 respectively. This highlights the need for multimodal characterization of these complex reactions. Formation of bicarbonate species likely follows the general reactions outlined in Eq. 5 and 6:

$$K_4H_2(CO_3)_3 \cdot 1.5H_2O + CO_2 \rightarrow 4KHCO_3 + 0.5H_2O \quad \text{Eq. 8}$$

50% relative humidity

The MCR-ALS analysis of the ATR IR spectra at 50% RH (**Figure 1b**) was the most challenging. Six spectral components were assigned and the results are shown in **Figures 2c** and **2d**. The assignments are consistent with μXRD and the MCR-ALS analyses of the 40% RH (above) and 60% RH (below). Increased H_2O uptake in the 50% versus 40% RH experiment required assignments of spectral components to both solid and solution phase species. For example, we assigned the first (50c1) and second (50c2) component to the solid $K_2Al_2O(OH)_6$ phase and its hydrated form, respectively; although, the second component (50c2) shows additional weak and broad signals between 1350 and 1700 cm^{-1} that might represent a small contribution from an aqueous carbonate anion. Similarly, the fifth (50c5) and sixth (50c6) components are attributed to the aqueous bicarbonate anion, $HCO_{3\,(aq)}^-$ and solid potassium bicarbonate $KHCO_3$, respectively. These assignments are based on and presence of characteristic bands in the 1370, 1600, 2600 cm^{-1} region corresponding to the ν_4 C-O-H bend, ν_2 CO_2 asymmetric stretch/H_2O bend, and O-H stretching vibrational modes,[43, 44] respectively, and are consistent with $KHCO_3$

detected by μXRD (**Table 1**). The third (50c3) and fourth (50c4) components are assigned to the aqueous carbonate, $CO_3^{2-}{}_{(aq)}$ and $KAl(CO_3)(OH)_2$, respectively in accordance with 40% RH results (see above). Dominance of bicarbonate species in the products indicates further acidification with respect to the system at 40% RH from pH < 10 to 7 < pH < 8.[38]

As in the 40% RH system, the decrease in the relative concentration of $K_2Al_2O(OH)_6$ (50c1 and 50c2) at 50% RH (**Figure 2d**) corresponds with an increase in the relative concentration of $CO_3^{2-}{}_{(aq)}$ (50c3) and $KAl(CO_3)(OH)_2$ (50c4). However, the relative concentration of $KAl(CO_3)(OH)_2$ (50c4) is notably lower than in the 40% RH system, and the dominant species in later stages of the reaction (>20 hrs) are the solvated (50c5) and solid bicarbonate species (50c6). The reactions in Eq. 1-8 account for all species observed in the 50% RH ATR IR spectra, but with the different carbonate speciation progressing towards $KHCO_3$ (Eq. 8).

The μXRD results (**Table 1**) confirm the presence of $KAl(CO_3)(OH)_2$ (50c4) and $KHCO_3$ (50c6) in the reaction products at 50% RH (**Figure 2d**). Additional phases identified by μXRD include $K_4H_2(CO_3)_3{\cdot}1.5H_2O$, in accordance with the equilibria described in Eq. 6, and gibbsite (**Figure S6**), although no unique spectral component from the MCR-ALS analysis could be assigned to these species (**Table 1**, **Figure S4**).

60% relative humidity

Four spectral components were assigned in the MCR-ALS analysis of the ATR IR spectra at 60% RH (**Figure 1c**), and their spectra are shown in **Figure 2e**. The first two components (60c1 and 60c2) are assigned to solid $K_2Al_2O(OH)_6$ and its hydrated form, respectively. Absorbance between 1350 and 1550 cm^{-1} suggests a contribution from $CO_3^{2-}{}_{(aq)}$ in component 60c2, but most of the $CO_3^{2-}{}_{(aq)}$ signal was accounted by component 60c3. Time-resolved changes in relative concentrations (**Figure 2f**) reveal fast hydration of $K_2Al_2O(OH)_6$ (60c1 to 60c2 in <2 hrs), followed by rapid decomposition of the dimer and reaction with dissociated carbonic acid to form $CO_3^{2-}{}_{(aq)}$ (60c3). Transformation of $K_2Al_2O(OH)_6$ to aqueous carbonate is consistent with equilibria described in Eq. 1 and 2. Upon reaching a maximum concentration at ca. 10 hrs, $CO_3^{2-}{}_{(aq)}$ (60c3) is subsequently replaced with $KHCO_3$ (60c4) (Eq. 5,6 and 8). The μXRD analysis (**Table 1**) of the post-reacted sample from the 60% RH experiment confirms the presence of $KHCO_3$ (60c4), and

gibbsite as the sole Al-bearing product. In this case, the ATR IR spectrum at the end of the 60% RH experiment (**Figure S7**) shows peaks at ca. 3525 and 3620 cm^{-1}, and weak but discernable shoulders at ca. 3380, 3395, and 3450 cm^{-1}, consistent with the unique OH stretches of the aluminum hydroxide phase.[39] Presence of both carbonate and bicarbonate species in the early stages of reaction and dominance of bicarbonate species in the final stages of the reaction pathway indicates change from pH > 9 to 7 < pH < 8. Furthermore, absence of K-dawsonite from the products identified via μ-XRD indicates that the final pH of the system is shifting towards neutral conditions as RH increases.

Reactivity trends and their implications

The presence of H_2O plays a key role in the evolution of products formed from the tetrahedrally coordinated aluminate dimer, $K_2Al_2O(OH)_6$ and, in its absence, CO_2 does not react with the aluminate phase. The amount of available H_2O dictates the rate of reaction, as demonstrated by results obtained from 20 and 30% RH experiments (see **Supporting Information**) which were monitored for 21 and 11 days, respectively, before resulting solids were subjected to μXRD analysis. Despite the significantly longer exposure times than those for RH>30%, $K_2Al_2O(OH)_6$ remained the major solid phase (**Figure S4**).

The evolution of different species followed the same initial path, with simultaneous decomposition of $K_2Al_2O(OH)_6$ and growth of $CO_3^{2-}{}_{(aq)}$. The nature of the amorphous aluminum phase in Eq. 1 remains unknown, but formation of gibbsite at this stage is unlikely. Experiments conducted at lower RH conditions are representative of the early stages of $K_2Al_2O(OH)_6$ reaction and no gibbsite peaks were present in the μXRD patterns (**Figure S4**). After initial depletion of $K_2Al_2O(OH)_6$ and formation of $CO_3^{2-}{}_{(aq)}$, the amount of H_2O present dictates the reaction pathway.

Introduction of H_2O into the $K_2Al_2(OH)_6$-CO_2 system is crucial as it initiates a chain reaction starting with formation of KOH and K_2CO_3 in accordance with Eq. 1-2. Presence of these species allows for different reaction pathways and products, each driven by the availability of H_2O. At low H_2O content, formation of the activated/hydrated form of K_2CO_3 (i.e. $K_2CO_3{\cdot}1.5H_2O$) is limited, resulting in diminished reactivity towards available CO_2 and consequent neutralization of the systems alkaline pH according to Eq. 5, 6 and 8.[45] Availability of carbonate anions under

these conditions in solvated, solid, or hydrated form promotes reaction with the aluminum intermediate to yield $KAl(CO_3)(OH)_2$ (Eq. 3). As humidity increases, formation of $K_2CO_3{\cdot}1.5H_2O$ becomes more favorable resulting in overall drop in the pH of the system over time due to depletion of carbonate species formed from the limited supply of $K_2Al_2(OH)_6$ (Eq. 1-2). The relatively more acidic conditions, paired with decreased availability of carbonate anions result in formation of gibbsite as the sole Al-bearing phase. This is consistent with trends in gibbsite synthesis that utilize near-neutral to acidic conditions.[46]

These results provide insight into the formation of indurated crusts on highly alkaline Na-rich radioactive tank wastes with long exposures to ambient air, such as those at Hanford.[47] Despite the more complex chemistry in the tanks, transformation of the Na-bearing carbonate mineral thermonatrite ($Na_2CO_3{\cdot}H_2O$) and gibbsite ($Al(OH)_3$)) , to trona, $Na_2(CO_3){\cdot}Na(HCO_3){\cdot}2H_2O$ and dawsonite ($NaAlCO_3(OH)_2$) are similar to their K-bearing counterparts, $K_2CO_3{\cdot}1.5H_2O$ and $K_4H_2(CO_3)_3{\cdot}1.5H_2O$, studied here.[11] This suggests that the change likely occurred in the tanks at 40-50% RH where both mixed carbonate/bicarbonate species would exist in addition to dawsonite (**Table 1**). Further studies will address the effect of temperature on reaction rates, the role of the counter cation (Na^+ vs. K^+) in reaction product formation, and the coordination environment of transient Al species.

Conclusions

This study highlights the effects of atmosphere, in the form of constant CO_2 concentration (400 ppm) and variable humidity, on the identity of products formed from the tetrahedral aluminate dimer, $K_2Al_2O(OH)_6$. A multimodal characterization approach, consisting of in-situ ATR IR measurements, post-reaction ex-situ μ-XRD analysis, and MCR-ALS chemometrics analysis, provided unprecedented insights into the nature of intermediates and products formed under different humidity conditions. Identification of crystalline phases present at the end of the reaction using μ-XRD allowed for accurate and informed decomposition of complex time-resolved IR data, showing the commanding role of humidity in initiating the reaction and influencing the nature of the products formed. General reactivity trends show a positive correlation between the RH and reaction kinetics, as demonstrated by negligible reaction

progress after 21 days at 20% RH, and complete reaction after only 4 days at 60% RH. The amount of available H_2O is closely correlated to the carbonate/bicarbonate speciation. Lower RH conditions favored carbonate containing products, including incorporation of carbonate into the Al-bearing phase, $KAl(CO_3)(OH)_2$. Higher RH conditions resulted in products dominated by bicarbonate, and the carbonate free Al-phase, gibbsite ($Al(OH_3)$). The pH conditions, elucidated from carbonate/bicarbonate equilibria, indicate an overall shift from initially alkaline to near neutral conditions, with enhanced acidification of the system as a function of higher humidity and dissolved CO_2. Near neutral conditions are favorable to the formation of six-coordinate Al intermediates, with $KAl(CO_3)(OH)_2$ and/or $Al(OH)_3$ ultimately precipitating as the final products. This surface-mediated transformation mechanism provides an alternative pathway for precipitation of six-coordinate Al phases from formally four-coordinate aluminate monomers and dimers. Our findings suggest that humidity can be used to tune the nature of the reaction product during Al transformation, which is of use to the Al processing industry, and to the retrieval and processing of caustic Al-bearing radioactive waste solutions.

Acknowledgements

This research was supported by IDREAM (Interfacial Dynamics in Radioactive Environments and Materials), an Energy Frontier Research Center funded by the U.S. Department of Energy (DOE) Office of Science, Basic Energy Sciences (BES). A portion of the research was conducted at the Environmental Molecular Science Laboratory (EMSL, grid.436923.9), a DOE Office of Science User Facility sponsored by the Office of Biological and Environmental Research at Pacific Northwest National Laboratory (PNNL). PNNL is a multiprogram national laboratory operated for DOE by Battelle Memorial Institute operating under Contract No. DE-AC05-76RL0-1830.

References

1. Den Hond, R.; Hiralal, I.; Rijkeboer, A., Alumina Yield in the Bayer Process Past, Present and Prospects. In *Essential Readings in Light Metals: Volume 1 Alumina and Bauxite*, Donaldson, D.; Raahauge, B. E., Eds. Springer International Publishing: Cham, 2016; pp 528-533.
2. Gontijo, G. S.; de Araujo, A. C. B.; Prasad, S.; Vasconcelos, L. G. S.; Alves, J. J. N.; Brito, R. P., Improving the Bayer Process productivity - An industrial case study. *Miner Eng* **2009,** *22*, 1130-1136.
3. Misra, C.; White, E. T., Crystallisation of Bayer Aluminium Trihydroxide. *J Cryst Growth* **1971,** *8* (2), 172-&.
4. Herting, D. L.; Reynolds, J. G.; Barton, W. B., Conversion of Coarse Gibbsite Remaining in Hanford Nuclear Waste Tank Heels to Solid Sodium Aluminate [$NaAl(OH)_4 \cdot 1.5H_2O$]. *Ind Eng Chem Res* **2014,** *53*, 13833-13842.
5. McGinnis, C. P.; Welch, T. D.; Hunt, R. D., Caustic leaching of high-level radioactive tank sludge: A critical literature review. *Separ Sci Technol* **1999,** *34*, 1479-1494.
6. Colburn, H. A.; Peterson, R. A., A history of Hanford tank waste, implications for waste treatment, and disposal. *Environ Prog Sustain* **2020**.
7. Gephart, R. E., A short history of waste management at the Hanford Site. *Phys Chem Earth* **2010,** *35*, 298-306.
8. Hill, R. C. P.; Reynolds, J. G.; Rutland, P. L. *A Comparison of Hanford and Savannah River Site High-Level Wastes*. Proceedings of the 13th International High-Level Waste Management Conference, 114-117, American Nuclear Society, La Grange Park, Il.
9. Kupfer, M.; Boldt, A., 1997. Standard Inventories of Chemicals and Radionuclides in Hanford Site Tank Wastes. Westinghouse Hanford Company, Richland, WA.
10. Peterson, R. A.; Buck, E. C.; Chun, J.; Daniel, R. C.; Herting, D. L.; Ilton, E. S.; Lumetta, G. J.; Clark, S. B., Review of the Scientific Understanding of Radioactive Waste at the US DOE Hanford Site. *Environ Sci Technol* **2018,** *52*, 381-396.
11. Page, J. S.; Reynolds, J. G.; Ely, T. M.; Cooke, G. A., Development of a carbonate crust on alkaline nuclear waste sludge at the Hanford site. *Journal of Hazardous Materials* **2018,** *342*, 375-382.
12. Reynolds, J. G.; Cooke, G. A.; Herting, D. L.; Warrant, R. W., Evidence for dawsonite in Hanford high-level nuclear waste tanks. *Journal of Hazardous Materials* **2012,** *209*, 186-192.
13. Jiang, Y. F.; Liu, C. L.; Xue, J.; Li, P.; Yu, J. G., Insights into the polymorphic transformation mechanism of aluminum hydroxide during carbonation of potassium aluminate solution. *Crystengcomm* **2018,** *20*, 1431-1442.
14. Li, Y.; Zhang, Y. F.; Chen, F. F.; Yang, C.; Zhang, Y., Polymorphic Transformation of Aluminum Hydroxide Precipitated from Reactive NaAl(OH)(4)-NaHCO3 Solution. *Cryst Growth Des* **2011,** *11*, 1208-1214.
15. You, S. W.; Li, Y.; Zhang, Y. F.; Yang, C.; Zhang, Y., Synthesis of Uniformly Spherical Bayerite from a Sodium Aluminate Solution Reacted with Sodium Bicarbonate. *Ind Eng Chem Res* **2013,** *52*, 12710-12716.

16. Buvari-Barcza, A.; Rozsahegyi, M.; Barcza, L., Hydrogen bonded associates in the Bayer process (in concentrated aluminate lyes): the mechanism of gibbsite nucleation. *J Mater Chem* **1998,** *8*, 451-455.
17. Graham, T. R.; Dembowski, M.; Hu, J. Z.; Jaegers, N. R.; Zhang, X.; Clark, S. B.; Pearce, C. I.; Rosso, K. M., Intermediate Species in the Crystallization of Sodium Aluminate Hydroxy Hydrates. *J Phys Chem C* **2020,** *124*, 12337-12345.
18. Sipos, P.; Hefter, G.; May, P. M., Al-27 NMR and Raman spectroscopic studies of alkaline aluminate solutions with extremely high caustic content - Does the octahedral species $Al(OH)_6^{3-}$ exist in solution? *Talanta* **2006,** *70*, 761-765.
19. Akitt, J. W.; Gessner, W., Al-27 Nuclear Magnetic-Resonance Investigations of Highly Alkaline Aluminate Solutions. *J Chem Soc Dalton* **1984,** 2, 147-148.
20. Dembowski, M.; Graham, T. R.; Reynolds, J. G.; Clark, S. B.; Rosso, K. M.; Pearce, C. I., Influence of soluble oligomeric aluminum on precipitation in the Al–KOH–H2O system. *Physical Chemistry Chemical Physics* **2020,** *22*, 24677-24685.
21. Dembowski, M.; Prange, M. P.; Pouvreau, M.; Graham, T. R.; Bowden, M. E.; N'Diaye, A. T.; Schenter, G. K.; Clark, S. B.; Clark, A. E.; Rosso, K. M.; Pearce, C. I., Inference of Principal Species in Caustic Aluminate Solutions Through Solid-State Spectroscopic Characterization. *Dalton T* **2020**.
22. Hu, J. Z.; Zhang, X.; Jaegers, N. R.; Wan, C.; Graham, T. R.; Hu, M.; Pearce, C. I.; Felmy, A. R.; Clark, S. B.; Rosso, K. M., Transitions in Al Coordination during Gibbsite Crystallization Using High-Field Al-27 and Na-23 MAS NMR Spectroscopy. *J Phys Chem C* **2017,** *121*, 27555-27562.
23. Reynolds, D. A.; Reynolds, J. G., 2018. *Theory of Carbon Dioxide Absorption by Hanford Waste*, Proceedings of Waste Management 2018, Waste Management Symposia Inc, Phoenix, AZ.
24. Johansson, G., Crystal Structure of Potassium Aluminate K2[Al2O(OH)6]. *Acta Chem Scand* **1966,** *20*, 505-515.
25. de Juan, A.; Tauler, R., Multivariate curve resolution (MCR) from 2000: Progress in concepts and applications. *Crit Rev Anal Chem* **2006,** *36*, 163-176.
26. Gorzsás, A. MCR-ALS GUI v4c, Open source MATLAB script from the Vibrational Spectroscopy Core Facility, Umeå University, Umeå Sweden, https://www.umu.se/en/research/infrastructure/visp/downloads/.
27. Duncan, J. P.; Sackschewsky, M. R.; Tilden, H. T.; Moon, T.; Barnett, J. M.; Fritz, B.; Stoetzel, G.; Su-Coker, J.; Ballinger, M.; Becker, J. M. *Pacific Northwest National Laboratory Annual Site Environmental Report for Calendar Year 2015*; Pacific Northwest National Lab.(PNNL), Richland, WA (United States): 2016.
28. Pouvreau, M.; Dembowski, M.; Clark, S. B.; Reynolds, J. G.; Rosso, K. M.; Schenter, G. K.; Pearce, C. I.; Clark, A. E., Ab Initio Molecular Dynamics Reveal Spectroscopic Siblings and Ion Pairing as New Challenges for Elucidating Prenucleation Aluminum Speciation. *J Phys Chem B* **2018,** *122*, 7394-7402.
29. Baldassarre, M.; Barth, A., The carbonate/bicarbonate system as a pH indicator for infrared spectroscopy. *Analyst* **2014,** *139*, 2167-2176.

30. Joshi, S.; Kalyanasundaram, S.; Balasubramanian, V., Quantitative Analysis of Sodium Carbonate and Sodium Bicarbonate in Solid Mixtures Using Fourier Transform Infrared Spectroscopy (FT-IR). *Appl Spectrosc* **2013,** *67*, 841-845.
31. Adam, A.; Cirpus, V., Darstellung und Struktur der ersten gemischten Alkalimetallhydrogencarbonate $NaA_2[H(CO_3)_2]\cdot 2H_2O$ mit A= K, Rb. *Zeitschrift für anorganische und allgemeine Chemie* **1996,** *622*, 2023-2030.
32. Bertoluzza, A.; Monti, P.; Morelli, M. A.; Battaglia, M. A., A Raman and Infrared Spectroscopic Study of Compounds Characterized by Strong Hydrogen-Bonds. *J Mol Struct* **1981,** *73*, 19-29.
33. Fernandez-Carrasco, L.; Puertas, F.; Blanco-Varela, M. T.; Vazquez, T.; Rius, J., Synthesis and crystal structure solution of potassium dawsonite: An intermediate compound in the alkaline hydrolysis of calcium aluminate cements. *Cement Concrete Res* **2005,** *35*, 641-646.
34. Placencia-Gomez, E.; Kerisit, S. N.; Mehta, H. S.; Qafoku, O.; Thompson, C. J.; Graham, T. R.; Ilton, E.; Loring, J. S., Critical Water Coverage during Forsterite Carbonation in Thin Water Films: Activating Dissolution and Mass Transport. *Environ Sci Technol* **2020,** *54*, 6888-6899.
35. Roonasi, P.; Holmgren, A., An ATR–FTIR study of carbonate sorption onto magnetite. *Surface and Interface Analysis* **2010,** *42*, 1118-1121.
36. Serna, C. J.; Garciaramos, J. V.; Pena, M. J., Vibrational Study of Dawsonite Type Compounds $NaAl(OH)_2CO_3$, $KAl(OH)_2CO_3$, $NH_4Al(OH)_2CO_3$. *Spectrochim Acta A* **1985,** *41*, 697-702.
37. Garand, E.; Wende, T.; Goebbert, D. J.; Bergmann, R.; Meijer, G.; Neumark, D. M.; Asmis, K. R., Infrared Spectroscopy of Hydrated Bicarbonate Anion Clusters: $HCO_3^-(H_2O)_{1-10}$. *J Am Chem Soc* **2010,** *132*, 849-856.
38. Wolf-Gladrow, D. A.; Zeebe, R. E.; Klaas, C.; Kortzinger, A.; Dickson, A. G., Total alkalinity: The explicit conservative expression and its application to biogeochemical processes. *Mar Chem* **2007,** *106*, 287-300.
39. Wang, S. L.; Johnston, C. T., Assignment of the structural OH stretching bands of gibbsite. *Am Mineral* **2000,** *85*, 739-744.
40. Luo, H. C.; Chioyama, H.; Thurmer, S.; Ohba, T.; Kanoh, H., Kinetics and Structural Changes in CO_2 Capture of K_2CO_3 under a Moist Condition. *Energ Fuel* **2015,** *29*, 4472-4478.
41. Wang, S. Y.; Liu, Z. W.; Smith, A. T.; Zeng, Y. X.; Sun, L. Y.; Wang, W. X., Dry hydrated potassium carbonate for effective CO_2 capture. *Dalton T* **2020,** *49*, 3965-3969.
42. Veselovskaya, J. V.; Derevschikov, V. S.; Kardash, T. Y.; Stonkus, O. A.; Trubitsina, T. A.; Okunev, A. G., Direct CO_2 capture from ambient air using K_2CO_3/Al_2O_3 composite sorbent. *Int J Greenh Gas Con* **2013,** *17*, 332-340.
43. Dobson, K. D.; McQuillan, A. J., An infrared spectroscopic study of carbonate adsorption to zirconium dioxide sol-gel films from aqueous solutions. *Langmuir* **1997,** *13*, 3392-3396.
44. Rudolph, W. W.; Fischer, D.; Irmer, G., Vibrational spectroscopic studies and density functional theory calculations of speciation in the CO_2-water system. *Appl Spectrosc* **2006,** *60*, 130-144.

45. Lee, S. C.; Choi, B. Y.; Ryu, C. K.; Ahn, Y. S.; Lee, T. J.; Kim, J. C., The effect of water on the activation and the CO_2 capture capacities of alkali metal-based sorbents. *Korean Journal of Chemical Engineering* **2006,** *23*, 374-379.
46. Zhang, X.; Huestis, P. L.; Pearce, C. I.; Hu, J. Z.; Page, K.; Anovitz, L. M.; Aleksandrov, A. B.; Prange, M. P.; Kerisit, S.; Bowden, M. E.; Cui, W.; Wang, Z.; Jaegers, N. R.; Graham, T. R.; Dembowski, M.; Wang, H.-W.; Liu, J.; N'Diaye, A. T.; Bleuel, M.; Mildner, D. F. R.; Orlando, T. M.; Kimmel, G. A.; La Verne, J. A.; Clark, S. B.; Rosso, K. M., Boehmite and Gibbsite Nanoplates for the Synthesis of Advanced Alumina Products. *ACS Applied Nano Materials* **2018,** *1*, 7115-7128.
47. Reynolds, J. G., The apparent solubility of aluminum (III) in Hanford high-level waste. *J Environ Sci Heal A* **2012,** *47*, 2213-2218.